Molecular dynamic simulation of low-energy FIB irradiation induced damage in diamond

Zhen Tong[1*,3], Zongwei Xu[2], Wei Wu[2], Xichun Luo[3]

1 Center for Precision Engineering, Harbin Institute of Technology, Harbin 150001, China

2 Centre of MicroNano Manufacturing Technology, Tianjin University, Tianjin 300072, China

3 Centre for Precision Manufacturing, Department of Design, Manufacture & Engineering Management, University of Strathclyde, Glasgow G1 1XQ, UK

*Email: zhen.tong528@gmail.com

Abstract

In this article, a large scale multi-particle molecular dynamics (MD) simulation model was developed to study the dynamic structural changes in single crystal diamond under 5 keV Ga^+ irradiation in conjunction with a transmission electron microscopy (TEM) experiment. The results show that the thickness of ion-induced damaged layer (~ 9.0 nm) obtained from experiments and simulations has good accordance, which demonstrates the high accuracy achieved by the developed MD model. Using this model, the evolution of atomic defects, the spatial distributions of implanted Ga particles the thermal spike at the very core collision area were analysed. The local thermal recrystallizations observed during each single ion collision process and the increase of the density of the non-diamond phase (mostly sp^2 bonded) at irradiation area are fund to be the underling mechanisms responsible for ion fluence dependent amorphization of diamond observed in previous experiments.

(Some figures in this article are in colour only in the electronic version)

Keywords: molecular dynamics; focused ion beam; irradiation damage; amorphization; collision cascades.

Nomenclature

I	The ion beam current
d_{beam}	The ion beam diameter
V_{beam}	The accelerate voltage of ion beam
t_d	Dwell time
N_{Ga}	The number of incident Ga particles
E	The total energy of the system described by the Tersoff.ZBL potential
V_{ij}^{ZBL}	The ZBL portion of the Tersoff.ZBL potential function
$V_{ij}^{Tersoff}$	The Tersoff portion of the Tersoff.ZBL potential function
r_{ij}	The length of the ij bond
f_F	Fermi-like function
A_F	Parameters controls the transition between Tersoff and ZBL potentials
r_C	The cut-off distance for the ZBL potential
e	The unit electron charge
ε_0	The permittivity of vacuum
$\phi(r_{ij}/a)$	The ZBL universal screening function
f_R	The repulsive pair potential including two-body interaction
f_A	The attractive pair potential including three-body interactions
f_C	The smooth cut-off function to limit the range of the Tersoff potential
b_{ij}	The bond order term in Tersoff potential
A	The cohesion energy of the repulsive pair potential function
B	The cohesion energy of the attractive pair potential function
D	The cut-off distance of Tersoff potential in LAMMPS
S_i	The cut-off distance for specie i in Tersoff potential
S_j	The cut-off distance for specie j in Tersoff potential
R	The radius of first neighbour shell
β	The bond order parameter
λ_1	The slope parameter of the repulsive pair potential curve
λ_2	The slope parameter of the attractive pair potential curve
λ_3	The slope parameter of the cut-off potential function

c	The elastic parameter in Tersoff potential
d	The elastic constant in Tersoff potential
$\cos \theta_0$	The elastic constant in Tersoff potential
Z_i	The electron charge of the i-th atom nuclei from the Coulomb potential
Z_j	The electron charge of the j-th atom nuclei from the Coulomb potential
m, n	The high order constant in Tersoff potential
a_0	Lattice constant parameter for diamond

1. Introduction

Owing to unique material properties such as bio-compatibility, superior optical transmission rate, high PH/chemical surface sensitivity, and high radiation tolerance etc., diamond has been proposed as a promising material for applications such as quantum computers [1, 2], micro/nanoscale cutting tools [3-6], optical and electronic devices used in medical care and nuclear industry [7-9]. In all of these applications, a high-accuracy process technology is required to shape diamond with nanometre level precision.

Focused ion beam (FIB) system has been developed up-to-date as an indispensable tool to effectively process diamond for the fabrication of micro-cantilevers [10], three-dimensional (3D) nanostructures [11, 12], and preparation of specimen used in transmission electron microscopy (TEM) [13]. However, apart from the controlled removal of target material, the exposure of material to FIB (typically 2–30 kV) will result in surface and near-surface radiation damage due to the atomic displacements and the implantation of ion source material. This modification will alternate the surface composition, cause surface instability, and thus degrade the performance of the developed devices. For instance, the FIB-induced Ga doping and atomic defects around tool cutting edges were found to be the reason accounting for the initiation of micro diamond tool wear fabricated by FIB [14, 15], and low-energy FIB irradiation was recommended to minimise the damaged layer [14]. The alternation of the surface composition will change the ionization probability of the work material used in optics [16], and the highly doped region created by the implanted gallium dopants would lead to current leakage in quantum dot based devices [17]. Therefore, the knowledge of the fundamental physical aspects of ion-solid interactions leading to processing defects in diamond is significant to develop an effective way to control and minimise the formation of residual defects.

In recent years, a variety of experimental techniques including Raman spectroscopy [18], secondary ion mass spectrometry (SIMS) [16], and transmission electron microscope (TEM) [19, 20] have been used to study the ion-induced damage in diamond. Typically, Gnaser and

co-workers [16] has reported a fluence-dependent evolution of the implanted Ga concentration in nanocrystalline diamond films by SIMS. Rubanov *et al.* [19] and Mckenzie *et al.* [20] investigated the ion fluence-dependent amorphization of diamond substrate under 30 keV Ga[+] FIB milling. These experiments show the existence of atomic damaged layer in chemical vapour deposition (CVD) or doped diamond materials under high energy irradiation. However, little work has been found to characterise the FIB-induced damage on natural single crystal diamond under low-energy irradiation. Indeed, low-energy FIB irradiation is usually used to thin samples in a typical TEM study. The extra ion irradiation during the TEM sample preparation will cause the secondary ion damage in a target material and affect the accuracy of experimental measurements. Additionally, only the ion dose is measureable in a typical TEM experiment. The post-facto-observation leaves a gap in understanding dynamic ion-induced damage in diamond, forcing the use of assumptions.

On the other hand, molecular dynamic (MD) simulations constitute a powerful approach to address some fundamental issues of energetic ion bombardment [21-23]. Nordlund *et al.* [24] carried out a series of MD simulations to investigate the pre-existing point defect movement and annealing in collision cascades. Low-energy recoils (about 3–15 eV) can also lead to a significant athermal recrystallization of pre-existing damage [25]. Satake *et al.* [26] studied the influence of computational domain and empirical potential function on the accuracy of simulation results (40 keV Ga[+] impact silicon). Large-scale MD computational domain and a combination of ZBL (Ziegler, Biersack and Littmark) and Tersoff potential functions were reported to help express accurately the stopping of incident ions [26] and the fully track of the thermal spike [27]. Recently, the effects of ion fluence and acceleration energy of incident ion on the Si surface deformation have also been reported [28, 29]. These activities make it an interesting and important task to understand the fundamental effects of energetic particles on matter. However, due to the limitations of computer power, many previous MD simulation systems for tracking the evolution of amorphous zones in target materials are limited in scale

with inadequate experimental correlation. Little work has been done on the characterization of low-energy FIB irradiation induced damage in single crystal diamond.

In this paper, a large-scale MD multi-particle collision model was developed to emulate the lattice structural changes that lead to the formation of amorphous carbon layer in single crystal diamond under 5 keV Ga^+ irradiation. The evolution of atomic defects, thermal spike, and the distribution of implanted Ga were analysed. A TEM experiment was carried out to qualitatively validate the simulation results.

2. MD simulation

3.1 MD model of ion bombardment

In a typical ion collision process, each incident Ga ion will create a damaged region along its trajectory in target material. It is important to make sure that the system size is able to track all the stopping processes of incident particles as well as the entire collision cascades [27]. In this study, the system size and the boundary condition were determined by a numerical experimentation using a single ion collision model. As shown in figure 1 (b), the diamond workpiece model investigated in this study is a square box with a dimension of $50a_0 \times 50a_0 \times 60a_0$, composed of 1,217,161 atoms in total. The lattice constant a_0 is 3.567 Å for single crystal diamond. The three orientations of the workpiece are [1 0 0], [0 1 0] and [0 0 1] in the X, Y and Z directions, respectively (figure 1 (a)). Except the collision surface, all of the rest surfaces were built with a thermal layer with thicknesses of $2a_0$ to control the temperature at 297 K. Free boundary condition was used to avoid the reflection effect caused by using fixed or period boundary conditions.
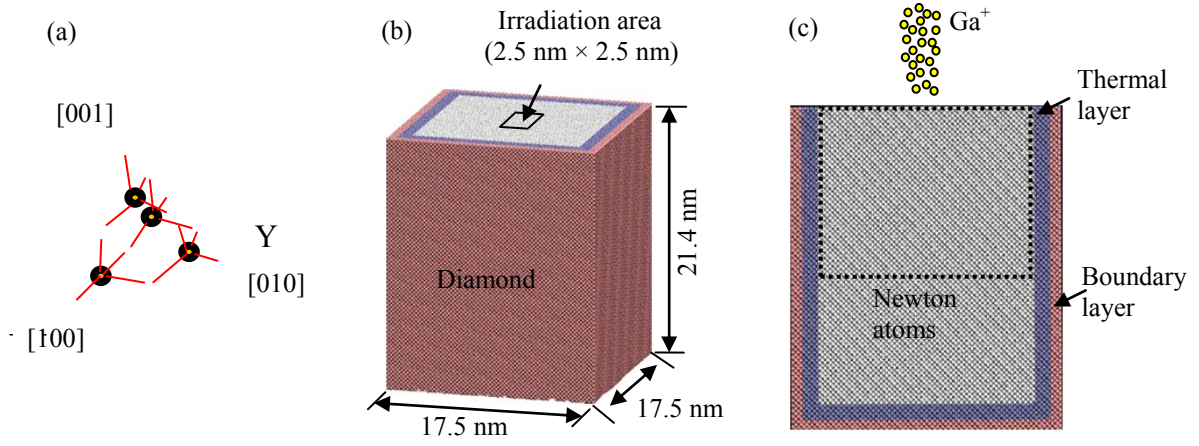
Figure 1: Multi-particle collision model: (a) the diamond crystalline lattice and the corresponding coordinate axes; (b) the dimensions of diamond bulk model; and (c) a cross-sectional view of the workpiece (The dotted line indicated the core collision area selected for local temperature analysis).

Another challenge to simulate the successive FIB milling process is how to describe the nature of ion beams. The flowchart of a program developed for building the multi-particle collision model is illustrated in figure 2. First of all, the ion dose was calculated according to the selected ion irradiation parameters such as the beam current I, the spot size d_{beam}, the acceleration voltage V_{beam} and the dwell time t_d. The total number of incident particles, N_{Ga}, can be calculated as follows:

$$N_{Ga} = \frac{I \times t_d}{e} \tag{1}$$

Then an algorithm was used to generate the initial coordinates for the N_{Ga} points having random distribution, and the coordinates were normalized to fit the defined sputter area of the MD model to avoid the overlap of atoms coordinates. In order to place the entire beam of particles in the MD simulation system but not have them adversely interacting, the incident particles are initially invisible to the system, having no mass, velocity, or potential with any of the C atoms in the

system as shown in figure 1 (c). The particles were then turned on, one by one, having the correct mass of gallium and the velocity corresponding to the energy of beam. The direction of incidence was perpendicular to the (0 0 1) surface of diamond, and the irradiation area was defined as 2.5 nm × 2.5 nm (figure 1 (b)).
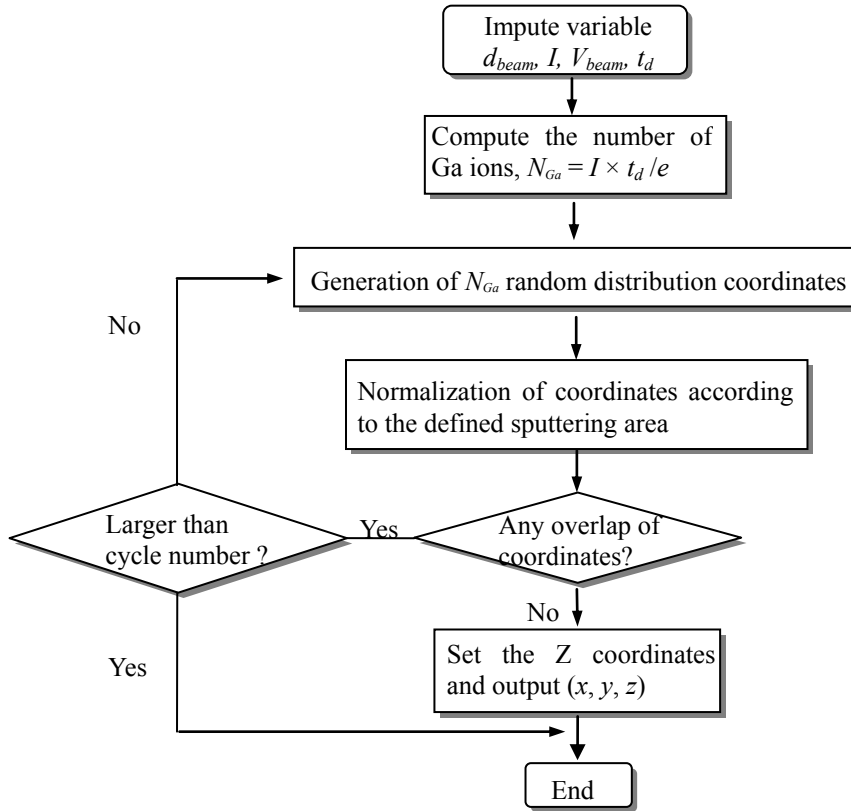

Figure 2: The program flowchart for building the coordinates of incident particles.

3.2 Potential functions

There are three different kinds of atomic interactions in the MD simulation: (1) the interaction between diamond atoms (C–C) in the workpiece; (2) the interaction between impact ions (Ga–Ga); (3) the interaction between Ga and diamond (Ga–C). In this research work, a combination of the Tersoff-potential [30] with the ZBL potential [31] was used to describe these interactions. The Tersoff.ZBL potential function includes a three-body Tersoff potential with a close-separation pairwise modification based on a Coulomb potential and the Ziegler-Biersack-Littmark universal screening function (ZBL potential function), giving the

energy E of a system of atoms as:

$$E = \frac{1}{2}\sum_{i}\sum_{j \neq i} V_{ij} \tag{2}$$

$$V_{ij} = (1 - f_F(r_{ij}))V_{ij}^{ZBL} + f_F(r_{ij})V_{ij}^{Tersoff} \tag{3}$$

$$f_F(r_{ij}) = \frac{1}{1 + e^{-A_F(r_{ij} - r_C)}} \tag{4}$$

where the V_{ij}^{ZBL} and $V_{ij}^{Tersoff}$ indicate ZBL portion and Tersoff portion, respectively. The distance between atoms i and j is r_{ij}. The f_F term is a fermi−like function used to smoothly connect the ZBL repulsive potential with the Tersoff potential. There are two parameters used to adjust it: A_F and r_C. A_F controls how "sharp" the transition is between the two portions, and r_C is essentially the cut-off distance for the ZBL potential.

For the ZBL portion, the interaction potential, V_{ij}^{ZBL}, between two atoms i and j can be written in the form of

$$V_{ij}^{ZBL} = \frac{1}{4\pi\varepsilon_0}\frac{Z_1 Z_2 e^2}{r_{ij}}\phi(r_{ij}/a) \tag{5}$$

where Z_1, Z_2 are the numbers of protons in each nucleus, e is the electron charge (1 for metal and real units) and ε_0 is the permittivity of vacuum. $\phi(r_{ij}/a)$ is the ZBL universal screening function.

For the Tersoff portion, the interaction potential, $V_{ij}^{Tersoff}$, between two atoms i and j can be computed as follows:

$$V_{ij}^{Tersoff} = f_C(r_{ij})[f_R(r_{ij}) + b_{ij}f_A(r_{ij})] \tag{6}$$

$$f_C(r) = \begin{cases} 1 : r < R - D \\ \frac{1}{2} - \frac{1}{2}\sin(\frac{\pi}{2}\frac{r - R}{D}) : R - D < r < R + D \\ 0 : r > R + D \end{cases} \tag{7}$$

$$f_R(r) = A\exp(-\lambda_1 r) \tag{8}$$

$$f_A(r) = -B\exp(-\lambda_2 r) \tag{9}$$

To the purpose of concision, the values of Tersoff.ZBL potential function parameters for pure C and Ga are listed in the table 1.

Table 1: Tersoff.ZBL potential function parameters for pure Ga and C

Parameters	Ga	C
m	1	1
c	7.6298×10^{-2}	1.9981×10^4
d	1.9796×10^1	7.0340
$\cos\theta_0$	7.1459×10^{-1}	-3.3953×10^{-1}
n	3.47290	9.9×10^{-1}
β	2.3586×10^{-1}	4.1612×10^{-6}
$A[eV]$	2.83982×10^3	1.5448×10^3
$B[eV]$	1.14786×10^2	3.8963×10^2
$D[\text{Å}]$	0.1	0.15
$\lambda_1[\text{Å}^{-1}]$	3.2834	3.4653
$\lambda_2[\text{Å}^{-1}]$	1.7154	2.3064
$\lambda_3[\text{Å}^{-1}]$	0	0
$R[\text{Å}]$	2.8	1.8
Z_i	31	6
Z_j	31	6

For the interaction between the diamond and gallium, the parameters values for species i and j were calculated using the mixing rules as list bellow:

$$\lambda_1^{i,j} = \frac{1}{2}(\lambda_1^i + \lambda_1^j) \tag{10}$$

$$\lambda_2^{i,j} = \frac{1}{2}(\lambda_2^i + \lambda_2^j) \tag{11}$$

$$A_{i,j} = (A_i A_j)^{\frac{1}{2}} \tag{12}$$

$$B_{i,j} = (B_i B_j)^{\frac{1}{2}} \tag{13}$$

$$R_{i,j} = (R_i R_j)^{\frac{1}{2}} \tag{14}$$

$$S_{i,j} = (S_i S_j)^{\frac{1}{2}} \tag{15}$$

3.3 MD simulation setup

MD simulations were implemented by using an open source code—LAMMPS [32]. The simulation was performed by high performance computing (HPC) platform using 32 cores. Before ion collision, 80,000 computing time steps were carried out to relax freely the system to 293 K. Since the high energetic ion collision process simulation is inherently a non-equilibrium event, the system was controlled by NVE ensemble [21]. The thermostat atoms were kept at a constant temperature of 293 K through velocity scaling method to perform the heat dissipation. The voltage of ion beam was assumed to be 5 kV in the simulation and it was translated into the velocity of gallium particles. It has been found through a "trial and error" approach that a time step of 0.1 fs is a good trade-off between computational efficiency and velocity insensitivity for the incident energy applied. After each ion collision the system was equilibrated via a velocity scaling stochastic layer until a point when the energy of the system has relaxed to a corresponding temperature of 293 K. The interval time between ion impacts was determined by a single ion collision event. An interval time of 18.0 ps was found to be sufficient to simulate the cooling process of the workpiece to a point when the energy of the workpiece system has relaxed to a corresponding temperature of 293 K. Additionally, the concept of atomistic equivalent temperature [33] was employed to characterise the local thermal spike during the ion collision process. The dotted line in figure 1 (c) indicated the core collision area selected for temperature analysis.

3. Experimental validation

In order to validate the developed MD simulation model, a TEM measurement was carried out to

characterise the damaged layer under 5 keV Ga^+ irradiation. A FEI Nova 200 nanolab dual beam FIB system with Ga ion source was used for both the ion irradiation in diamond and the TEM sample preparation. The SEM images showing the TEM sample preparation procedure are summarized in figure 3. The ion irradiation was carried out normal to the diamond (1 0 0) plane with an irradiation area of 10×10 μm^2 (figure 3 (a)). The applied ion fluence is 1.0×10^{18} ions/cm^2. After the irradiation the diamond sample was covered with Pt stripes deposited by using the standard e-beam deposition technique. The Pt stripes were used to avoid the charging effect and to protect the formed damage layer from additional Ga^+ irradiation during the following sample preparation procedure. The cross-sectional TEM sample was prepared using the standard lift-out technique described elsewhere [13] (figure 3 (b)-(c)). The sample was further thinning to electron transparency with the thickness less than 100 nm (figure 3 (d)). The TEM sample was examined using a FEI Tecnai TF20 TEM operated at 200 keV. Energy dispersive X-ray spectroscopy analysis (EDS) was performed to determine the relative gallium and carbon concentration near the surface.
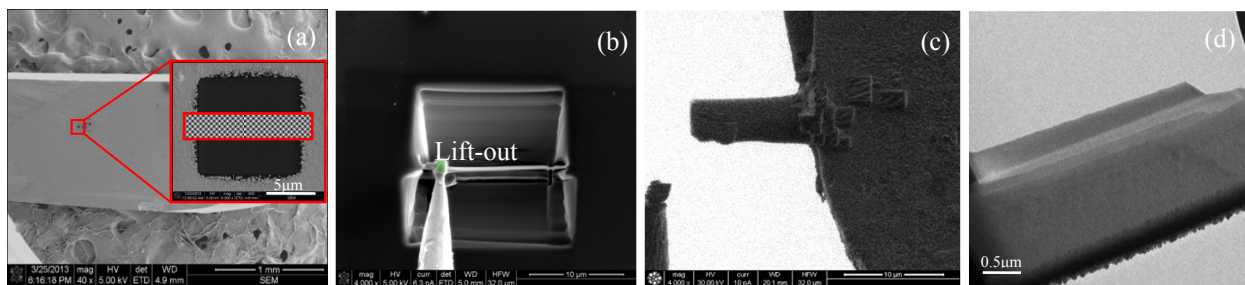

Figure 3: The SEM images showing the TEM sample preparation procedure. (a) Ion implantation; (b) Create the slice and lift-out; (c) Mounting to grid; (d) Finial thinning.

4. Results and discussions

4.1 The ion collision process in diamond

The local temperature and the collision-dynamics during the interaction of a single 5 keV gallium ion with the diamond are shown in figure 4. Each diamond atom was coloured by the atom's common neighbour analysis value. The cyan and purple atoms represent the dangling

bonded and sp^2 bonded C atoms respectively. The defect-free regions (sp^3 hybridization) were removed from the visualizations. It is found that the single ion collision process comprises a temperature spike portion (encircled by the dotted line in figure 4; magnified and shown in inset (a)) and a relatively long stage of recrystallization process (healing the atomic defects).

When an energetic ion particle enters into the solid, it transfers its energy and momentum to the target atoms and creates voids and interstitials in addition to surface sputtering. As shown in figure 4 (b), a large number of atomic defects (vacancies and interstitials) were created by breaking the local sp^3 bonds of diamond at initial collision stage. During this period, the Ga particle transfers its kinetic energy partly into thermal energy of the target material. At 0.036 ps, the temperature at the very core of the impact area reached a peak value of 1221.2 K. This highest local temperature region is located at the surface facing the ion beam irradiation as shown by the encircled white line in figure 4 (b). The temperature didn't exceed the melting (or sublimation) point of diamond and no visible liquid zone in diamond was detected. The heat rapidly dissipated to the diamond bulk due to high thermal conductivity of diamond. Also, the damage zone was observed to grow continuously through the displacement cascades. The peak disorder of the local lattice structure was found at 0.094 ps, at which the local temperature was found to be cooled down to 682.8 K (figure 4 (c)). This process is quite different from the single cluster collision, under which pronounced crater rims or hillocks are normally created [34-36].

After the damage zone reached the peak disorder there was a long stage of relaxation process. The local high temperature provided the thermal energy required for the atomic defects to partly anneal back to diamond structure. It was found that more than half of the dangling bonded and sp^2 bonded C atoms has annealed back to diamond structure (figure 4 (e)) after the full-relaxation-process, and finally only a few atomic defects remain in the sample, mostly sp^2 bonded. Thus, the low energy ion collision process undergoes a collision cascade leading to a peak disorder of the lattice structure, and a relatively long period recrystallization process which partly annealing of the atomic defects back to diamond structure.
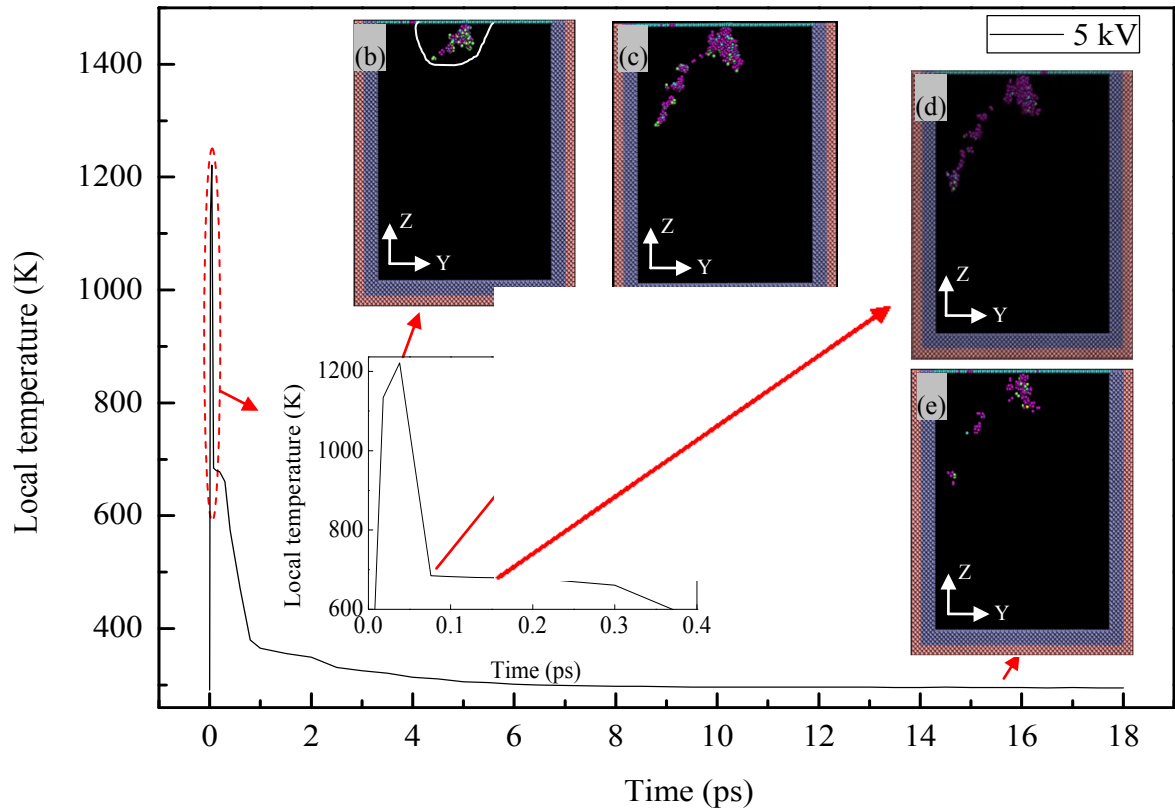
Figure 4: Molecular dynamics simulations describing the temperature evolution and the recrystallization process for the single Ga particle collision of diamond. Inset (a): the local view of the temperature during the temperature spike phase. Inset (b): the initial defects created when the local temperature has reached the peak value of 1221.2 K at 0.036 ps; this highest temperature region is shown by the encircled line. Inset (c): the defect configuration at the stage of the peak disorder of the lattice achieved at 0.094 ps. Inset (d): an intermediate phase during the recrystallization process observed at 0.15 ps; Ga particle stopped inside the diamond bulk at this stage. Inset (e): the residual atomic defects after the system cooled down to 293 K at 18.0 ps. The cyan atoms represent the dangling bonded C atoms and purple atoms represent sp^2 bonded C atoms. The C atoms of perfect diamond structure are removed from the visualizations.

4.2 The characterization of residual damage

Figure 5 shows the inside view of the atomic defects formed in diamond after 5 keV Ga$^+$ implantation with a fluence of 4.0 $\times 10^{14}$ ions/cm^2. As shown in figure 5 (a), the implanted

gallium ions create a damage region with a mean diameter of 5.0 nm, approximately an area of 19.6 nm^2, which is more than three times the irradiation area defined as 6.25 nm^2. The depth of the damaged region is 9.8 nm (figure 5 (b)). The distribution of all the implanted gallium ions (yellow colour) after the fully relaxation process are shown in figure 5 (c). The implanted gallium ions are uniformly distributed in the damaged layer after the low-energy irradiation. The maximum depth of the implanted Ga^+ was 9.1 nm.
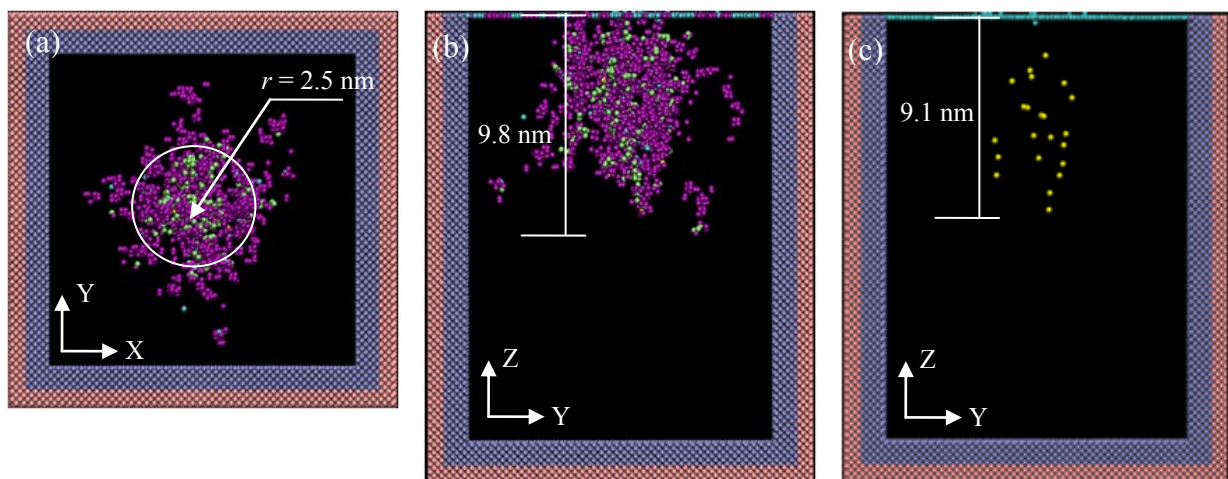
Figure 5: The internal images of the damaged area after 5 keV Ga^+ irradiation. (a) Plan view of amorphous region; (b) cross-section view of amorphous region; and (c) the distribution of the implanted gallium ions. The cyan atoms represent the 2-fold coordinated C atoms and purple atoms represent 3-fold coordinated C atoms. The yellow atoms represent the implanted gallium ions.

The ion-induced damage predicted by MD simulation was compared with the experimental results. The cross-sectional TEM image of the diamond sample after 5 keV Ga^+ irradiation is shown in figure 6 (a). Two white dotted lines were used to indicate the boundaries between the Pt layer, the damage layer, and the diamond bulk. The damage layer was clearly visible below the deposited Pt layer. Because the electrons will be scattered in arbitrary directions in amorphous materials, the absence of any diffraction contrast in the damage layer indicates that the layer is amorphous (marked as a-C). The measured thickness of the a-C layer is 9.0 nm which is slightly

smaller than the MD simulation predicted value.

Figure 6 (b) summarises the EDS depth profiling across the yellow line labelled "profile in (b)" shown in figure 6 (a). When the depth is less than 3.5 nm, there are strong signals of C, Ga, and Pt. This region can be identified as the extra damage caused by e-beam deposition of Pt. For the depth between 3.5 nm and 13 nm, there are strong signals of C and Ga, but a sharp reduction of the Pt signal. As the prefect diamond region should only consist of constant carbon signal, the presence of Ga signal strongly indicates that the damage layer caused by low energy Ga^+ implantation accommodates a significant proportion of the implanted Ga particles. Across this depth range, there is a great rise of the C signal whilst the Ga signal is largely reduced. When the depth is larger than 28.0 nm, the C signal turns to be constant whilst the Pt and Ga signals become extremely week, indicating that the material now is undamaged diamond. The Ga and Pt signals observed in diamond bulk (depths between 15.0–40.0 nm) were attributed to the additional implantation created during the thinning process when preparing the TEM sample. Therefore, the simulated results of the characterization of the damage region compare closely with the corresponding data derived from experiments, which well demonstrated the high accuracy achieved by the proposed MD model.
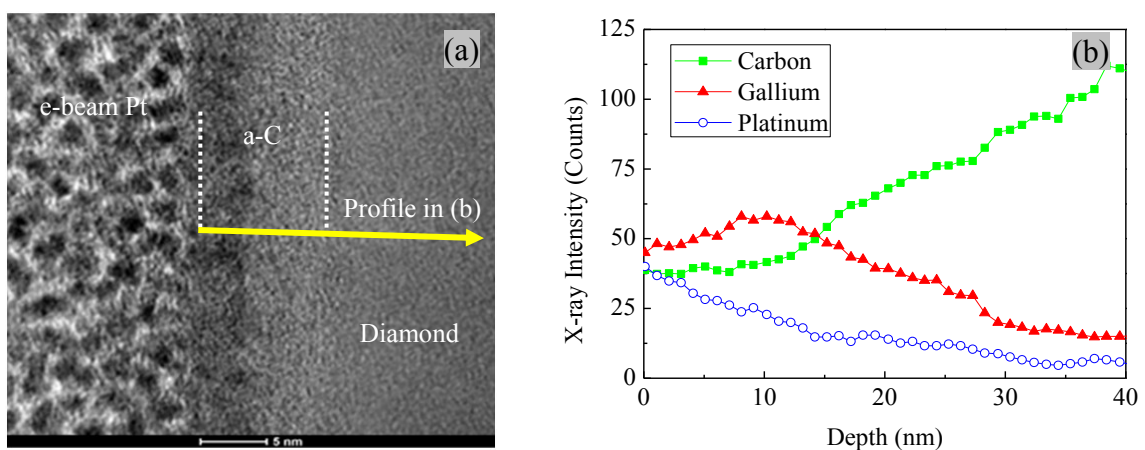

Figure 6: (a) TEM images of damage region after 5 keV Ga^+ irradiation with fluence of 1.0×10^{18} ions/cm^2. (b) The EDS depth profiling across the yellow line labelled "profile in (b)" shown in figure 6 (a).

4.3 The dynamic damage process

Using the MD model, the dynamic formation of atomic defects leading to the creation of residual damage layer inside diamond was further analysed. It is found that with the increase of ion dose, the atomic defects created inside the diamond matrix undergo a non-linear accumulation process. Figure 7 summarises the yields of sp^2 bonded atoms created by each ion collision. It is found that the increment of sp^2 bonded C atoms gradually decreases and approaches a stable value, nearly half of the first ion collision. The variation of the yield of atomic defects is mainly due to the fact that the atomic defects formed by the impact of the former ion will get annealed in part during the subsequent ion collision process.

To some extent, the number of the sp^2 bonded C atoms reflects the level of amorphization of residual damage layer. In this work, the component of a-C was further quantified by calculating the proportion of the sp^2 to sp^3 hybridization (sp^2/sp^3) within the damage region. The dashed line was used as a reference line to indicate the change of the rate of increase (as shown in figure 8). It is found that the sp^2/sp^3 is essentially increasing linearly with the ion fluence up to a value of 1.5×10^{14} ions/cm^2; above this ion fluence the slope of the curve gradually reduced. This non-liner increment of the sp^2/sp^3 indicated that the damage layer is not a simple accumulation of the defects created by each ion collision. Apart from the effect of local thermal recrystallization, another important factor responsible for this change is the increase of the local density of the non-diamond phase. The saturation of the non-diamond phase would suppress the formation of new defects. Additionally, the formation of atomic defects would also result in the alternation of the local physical and chemical properties of diamond, and change in the ion sputter yield. It is therefore anticipated that after reaching a critical ion dose, at which the increased material removal rate reaches the damage formation rate, a stabilization of the a-C layer is likely to be obtained.

Most recently, few attempts have been made study the ion-induced amorphization of diamond. Mckenzie *et al*. [20] has recently reported that the near-surface microstructure varies with the

increase of ion dose and the critical dose for the amorphization of the diamond surface is 2.0 × 10^{14} ions/cm^2 under 30 keV Ga$^+$ irradiation. For another study of 30 keV Ga$^+$ sputtered nanocrystalline diamond films, the thickness of the damage layer was found to grow with the ion dose and achieved an equilibrium value of 44 nm [16]. The ion fluence dependent amorphization of diamond observed in these experiments qualitatively support the dynamic equilibrium damage process obtained in the present MD simulation.

Therefore, conclusion can be drawn that the damage layer created by low energy FIB irradiation is a dynamic accumulation of the atomic defects created by each single ion collision. The dynamic damage process described in this study provides atomic insights into this dynamic process. The local thermal recrystallization observed during each single ion collision process and the increase of the density of the non-diamond phase at irradiation area are found to be the underling mechanisms responsible for ion fluence dependent amorphization of diamond observed in experiments.
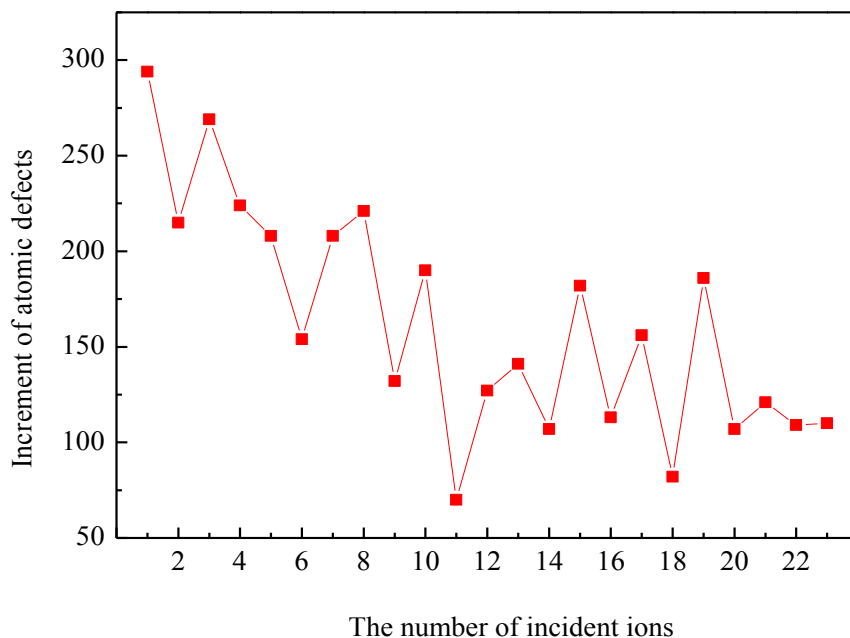

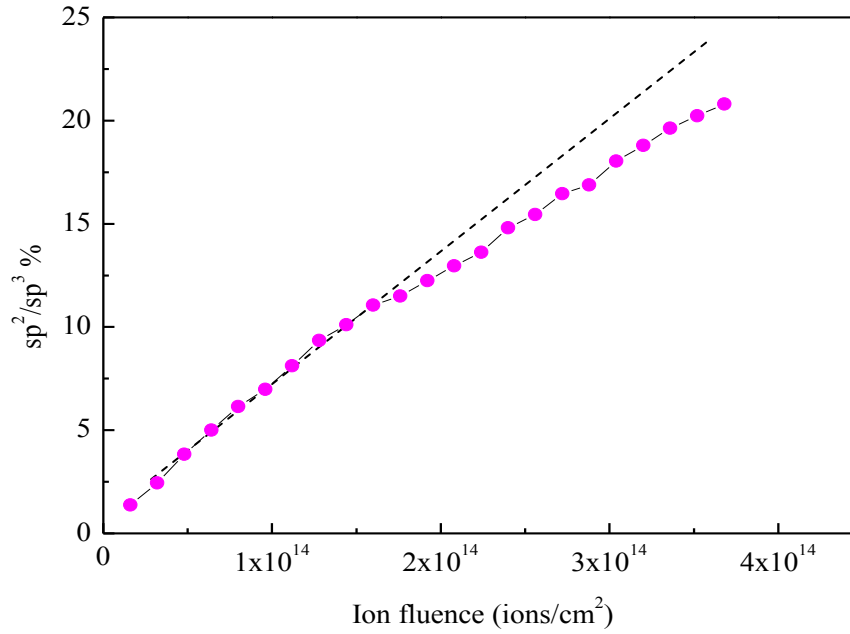**Figure 7:** The yield of the three-fold coordinated atoms for each ion collision.

Figure 8: The variation of the proportion of sp^2/sp^3 with the ion fluence.

5. Conclusions

In this work, a large-scale multi-particle collision model was developed to emulate the formation of amorphous carbon layer in the single crystal diamond which undergoes 5 keV Ga^+ implantation. The characteristic of residual damage predicated by the MD simulation has been compared with the TEM experiment.

The simulation results generally display good agreement with the experimental results. The measured and simulated thicknesses of damage layer are in good agreement. The residual damage layer formed after irradiation is a mixture phase of the sp^2 and sp^3 hybridization and accommodates a significant proportion of the implanted Ga particles. The damage layer was directly formed by the impacts of ions. No liquid flow phenomenon was detected under the applied beam voltage. The ratio of sp^2 to sp^3 increased with the ion fluence and approached a stable value, indicating the dynamic damage process in low energy implantation. The local thermal recrystallization observed during each single ion collision process and the increase of the density of the non-diamond phase at irradiation area are expected to be the underling mechanisms responsible for ion fluence dependent amorphization of diamond observed in

experiments.

Therefore, the multi-particle model appears to be well suited to investigate the energetic ion collision process in diamond. In the future, the model can be extended to account for V-shape formation as well as thermal annealing process under different irradiation conditions, so as to allow the comparison with a wider range of experimental data. Such investigations are presently under way.

Acknowledgment

References

[1]   T. Gaebel, M. Domhan, I. Popa, C. Wittmann, P. Neumann, F. Jelezko, *et al.*, "Room-temperature coherent coupling of single spins in diamond," *Nature Physics,* vol. 2, pp. 408-413, 2006.

[2]   A. D. Greentree, P. Olivero, M. Draganski, E. Trajkov, J. R. Rabeau, P. Reichart, *et al.*, "Critical components for diamond-based quantum coherent devices," *Journal of Physics: Condensed Matter,* vol. 18, p. S825, 2006.

[3]   D. Adams, M. Vasile, T. Mayer, and V. Hodges, "Focused ion beam milling of diamond: effects of H 2 O on yield, surface morphology and microstructure," *Journal of Vacuum Science & Technology B: Microelectronics and Nanometer Structures,* vol. 21, pp. 2334-2343, 2003.

[4]   X. Ding, G. Lim, C. Cheng, D. L. Butler, K. Shaw, K. Liu, *et al.*, "Fabrication of a micro-size diamond tool using a focused ion beam," *Journal of Micromechanics and Microengineering,* vol. 18, p. 075017, 2008.

[5]   Z. Xu, F. Fang, S. Zhang, X. Zhang, X. Hu, Y. Fu, *et al.*, "Fabrication of micro DOE using micro tools shaped with focused ion beam," *Optics express,* vol. 18, pp. 8025-8032, 2010.

[6]   J. Sun, X. Luo, W. Chang, J. Ritchie, J. Chien, and A. Lee, "Fabrication of periodic nanostructures by single-point diamond turning with focused ion beam built tool tips," *Journal of Micromechanics and Microengineering,* vol. 22, p. 115014, 2012.

[7]   A. Lohstroh, P. Sellin, S. Gkoumas, H. Al-Barakaty, P. Veeramani, M. Özsan, *et al.*, "The effect of fast neutron irradiation on the performance of synthetic single crystal diamond particle detectors," *Diamond and Related Materials,* vol. 19, pp. 841-845, 2010.

[8]   A. V. Sumant, O. Auciello, R. W. Carpick, S. Srinivasan, and J. E. Butler, "Ultrananocrystalline and nanocrystalline diamond thin films for MEMS/NEMS applications," *MRS bulletin,* vol. 35, pp. 281-288,

2010.

[9]   Ľ. Švorc, D. M. Stanković, and K. Kalcher, "Boron-doped diamond electrochemical sensor for sensitive determination of nicotine in tobacco products and anti-smoking pharmaceuticals," *Diamond and Related Materials,* vol. 42, pp. 1-7, 2014.

[10]   B. Z. Kupfer, R. K. Ahmad, A. Zainal, and R. B. Jackman, "Fabrication and characterisation of triangle-faced single crystal diamond micro-cantilevers," *Diamond and Related Materials,* vol. 19, pp. 742-747, 2010.

[11]   X. Luo, Z. Tong, and Y. Liang, "Investigation of the shape transferability of nanoscale multi-tip diamond tools in the diamond turning of nanostructures," *Applied Surface Science,* vol. 321, pp. 495-502, 2014.

[12]   J. Sun and X. Luo, *Deterministic Fabrication of Micro-and Nanostructures by Focused Ion Beam*: Springer, 2013.

[13]   D. Hickey, E. Kuryliw, K. Siebein, K. Jones, R. Chodelka, and R. Elliman, "Cross-sectional transmission electron microscopy method and studies of implant damage in single crystal diamond," *Journal of Vacuum Science & Technology A,* vol. 24, pp. 1302-1307, 2006.

[14]   W. Wu, Z. Xu, F. Fang, B. Liu, Y. Xiao, J. Chen*, et al.*, "Decrease of FIB-induced lateral damage for diamond tool used in nano cutting," *Nuclear Instruments and Methods in Physics Research Section B: Beam Interactions with Materials and Atoms,* vol. 330, pp. 91-98, 2014.

[15]   N. Kawasegi, K. Ozaki, N. Morita, K. Nishimura, and H. Sasaoka, "Single-crystal diamond tools formed using a focused ion beam: Tool life enhancement via heat treatment," *Diamond and Related Materials,* vol. 49, pp. 14-18, 2014.

[16]   H. Gnaser, B. Reuscher, and A. Brodyanski, "Focused ion beam implantation of Ga in nanocrystalline diamond: Fluence-dependent retention and sputtering," *Nuclear Instruments and Methods in Physics Research Section B: Beam Interactions with Materials and Atoms,* vol. 266, pp. 1666-1670, 2008.

[17]   D. D. Cheam, K. A. Walczak, M. Archaya, C. R. Friedrich, and P. L. Bergstrom, "Leakage current in single electron device due to implanted gallium dopants by focus ion beam," *Microelectronic Engineering,* vol. 88, pp. 1906-1909, 2011.

[18]   R. Brunetto, G. A. Baratta, and G. Strazzulla, "Amorphization of diamond by ion irradiation: a Raman study," in *Journal of Physics: Conference Series*, 2005, p. 120.

[19]   S. Rubanov and A. Suvorova, "Ion implantation in diamond using 30keV Ga+ focused ion beam," *Diamond and Related Materials,* vol. 20, pp. 1160-1164, 2011.

[20]   W. McKenzie, M. Z. Quadir, M. Gass, and P. Munroe, "Focused ion beam implantation of diamond," *Diamond and Related Materials,* vol. 20, pp. 1125-1128, 2011.

[21]   K. Nordlund, "Atomistic simulation of radiation effects in carbon-based materials and nitrides," *Nuclear Instruments and Methods in Physics Research Section B: Beam Interactions with Materials and Atoms,* vol. 218, pp. 9-18, 2004.

[22]   K. Nordlund, "Computational materials science of ion irradiation," *Nuclear Instruments and Methods in Physics Research Section B: Beam Interactions with Materials and Atoms,* vol. 188, pp. 41-48, 2002.

[23]   K. Nordlund, "Molecular dynamics simulation of ion ranges in the 1–100 keV energy range," *Computational materials science,* vol. 3, pp. 448-456, 1995.

[24]   K. Nordlund and R. Averback, "Point defect movement and annealing in collision cascades," *Physical Review B,* vol. 56, p. 2421, 1997.

[25]   J. Nord, K. Nordlund, and J. Keinonen, "Amorphization mechanism and defect structures in ion-beam-amorphized Si, Ge, and GaAs," *Physical Review B,* vol. 65, p. 165329, 2002.

[26]   S. Satake, N. Inoue, J. Taniguchi, and M. Shibahara, "Molecular dynamics simulation for focused ion beam processing: a comparison between computational domain and potential energy," in *Journal of Physics: Conference Series*, 2008, p. 012013.

[27]   R. Smith, S. D. Kenny, and D. Ramasawmy, "Molecular-dynamics simulations of sputtering," *Philosophical Transactions of the Royal Society of London. Series A: Mathematical, Physical and Engineering Sciences,* vol. 362, pp. 157-176, 2004.

[28]   S. Satake, S. Momota, S. Yamashina, M. Shibahara, and J. Taniguchi, "Surface deformation of Ar+ ion collision process via molecular dynamics simulation with comparison to experiment," *Journal of Applied Physics,* vol. 106, p. 044910, 2009.

[29]   S. Satake, S. Momota, A. Fukushige, S. Yamashina, M. Shibahara, and J. Taniguchi, "Molecular dynamics simulation of surface deformation via Ar+ ion collision process," *Nuclear Instruments and Methods in Physics Research Section B: Beam Interactions with Materials and Atoms,* vol. 272, pp. 5-8, 2012.

[30]   J. Tersoff, "Modeling solid-state chemistry: Interatomic potentials for multicomponent systems," *Physical Review B,* vol. 39, p. 5566, 1989.

[31]   J. F. Ziegler and J. P. Biersack, "The stopping and range of ions in matter," in *Treatise on Heavy-Ion Science*, ed: Springer, 1985, pp. 93-129.

[32]   S. Plimpton, "Fast parallel algorithms for short-range molecular dynamics," *Journal of computational physics,* vol. 117, pp. 1-19, 1995.

[33]   Z. Tong, Y. Liang, X. Yang, and X. Luo, "Investigation on the thermal effects during nanometric cutting process while using nanoscale diamond tools," *The International Journal of Advanced Manufacturing Technology,* pp. 1-10, 2014.

[34]   V. Popok, J. Samela, K. Nordlund, and V. P. Popov, "Impact of keV-energy argon clusters on diamond and graphite," *Nuclear Instruments and Methods in Physics Research Section B: Beam Interactions with Materials and Atoms,* vol. 282, pp. 112-115, 2012.

[35]   T. Aoki, T. Seki, and J. Matsuo, "Molecular dynamics study of crater formation by core-shell structured cluster impact," *Nuclear Instruments and Methods in Physics Research Section B: Beam Interactions with Materials and Atoms,* vol. 282, pp. 29-32, 2012.

[36]   V. N. Popok, I. Barke, E. E. Campbell, and K.-H. Meiwes-Broer, "Cluster–surface interaction: From soft landing to implantation," *Surface Science Reports,* vol. 66, pp. 347-377, 2011.